Fuel 381 (2025) 133429

Contents lists available at ScienceDirect

Fuel

journal homepage: www.elsevier.com/locate/fuel

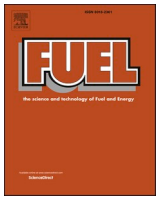

Full Length Article

# Wide-field imaging of gas-phase K species in biomass combustion using photofragmentation laser absorption imaging

Emil Thorin, Florian M. Schmidt *

*Thermochemical Energy Conversion Laboratory, Department of Applied Physics and Electronics, Umeå University, 90187 Umeå, Sweden*

ARTICLE INFO

*Keywords:*
Potassium (K)
Biomass combustion
Laser absorption imaging
Photofragmentation

ABSTRACT

Potassium (K) plays a key role in biomass combustion as its presence in the gas phase may lead to slagging, agglomeration and corrosion. To facilitate feedstock flexibility, a detailed understanding of the K chemistry during solid fuel conversion is needed. Here, we present photofragmentation laser absorption imaging for simultaneous, quantitative wide-field imaging of gaseous atomic K, potassium hydroxide (KOH) and potassium chloride (KCl) using a high-speed camera. Concentration images of the K species, at levels down to below parts-per-million, were acquired in a physical domain of 3.8-by-16.4 mm with a spatial resolution of 0.13 mm and a temporal resolution of 0.5 s after averaging. The technique was applied for imaging of the K species release from solid coffee husk and wheat straw samples combusted in a laboratory flame. Conversion of KCl salt was investigated as a reference. Significant differences in K species concentration and spatial distribution were observed between the fuels and between the devolatilization and char conversion stages. We also demonstrate spatial mapping of the atomic K fragment recombination rates with 1.2 μs time resolution, which constitutes a step towards reaction kinetics imaging.

## 1. Introduction

Biomass has received much attention as a renewable alternative to fossil fuels for combustion plants, which are vital components in the energy sector for district heating and electricity generation. The net carbon dioxide ($CO_2$) emissions from combustion of biomass fuels are low compared to fossil fuels and through carbon capture and storage (CCS), there is potential to reach net zero or negative $CO_2$ emissions [1,2]. However, the practical use of biomass as a fuel comes with challenges related to the ash-forming elements, specifically the highly abundant potassium (K). During solid fuel conversion, the majority of the K is released to the gas phase as potassium hydroxide (KOH), potassium chloride (KCl), and under certain conditions, as atomic K ($K_{at}$), which may cause slagging, sintering, deposit formation, high-temperature corrosion, and formation of hazardous particulate matter [3,4]. To mitigate the K related operational problems and utilize biomass fuels efficiently, a more detailed understanding of the K chemistry during solid fuel conversion is needed, including the gas phase chemistry. To this end, quantitative in situ measurements of the major gaseous K species are required, for which optical methods are suitable [5].

Solid fuel combustion is a dynamic process associated with both spatial and temporal variations, both of which can be resolved using imaging techniques. Van Eyk et al. employed a dye laser at 589.6 nm for quantitative imaging of atomic sodium (Na) above burning coal particles using laser-induced fluorescence (LIF) calibrated with absorption spectroscopy [6]. Following the work by van Eyk et al., Liu et al. employed LIF for imaging of $K_{at}$ surrounding burning biomass pellets by using an optical parametric oscillator (OPO) emitting pulses at 769.9 nm, targeting the D1 line of $K_{at}$ [7]. To image KOH and KCl during combustion of biomass pellets, Weng et al. employed laser-induced photofragmentation fluorescence (LIPF), where KOH and KCl were dissociated using a Nd:YAG laser at 266 nm and an ArF excimer laser at 193 nm, respectively, and the $K_{at}$ fluorescence following the fragmentation event was detected [8]. Despite the many advantages of fluorescence techniques, such as background-free signals, species selectivity, relative ease of implementation for imaging, and their wide applicability in combustion research, there are shortcomings, including self-absorption, collisional quenching and the need for calibration [9,10], which limit the ability for quantitative detection.

In an effort to enable fast, quantitative imaging, Wei et al. presented laser absorption imaging (LAI) of ethane ($C_2H_6$), carbon monoxide (CO),

* Corresponding author.
*E-mail address:* florian.schmidt@umu.se (F.M. Schmidt).

https://doi.org/10.1016/j.fuel.2024.133429
Received 2 July 2024; Received in revised form 23 September 2024; Accepted 11 October 2024
Available online 28 October 2024
0016-2361/© 2024 The Authors. Published by Elsevier Ltd. This is an open access article under the CC BY license (http://creativecommons.org/licenses/by/4.0/).

$CO_2$ and gas temperature in a laboratory flame using wavelength-tunable mid-infrared lasers (3–5 μm) [11]. This technique is a wide-field implementation of tunable diode laser absorption spectroscopy (TDLAS), where the incident laser wavelength is scanned across an absorption line of a target species, and the laser intensity is imaged by a high-speed camera to yield pixel-by-pixel absorption profiles. TDLAS has the advantage of being calibration-free, but unlike fluorescence imaging, a line-of-sight (LOS) projection of the analyte is obtained. However, tomographic algorithms can be applied to dissect the concentration profile along the LOS [11,12]. Thorin et al. recently applied tomographic LAI at 769.9 nm and 30 kHz camera frame rate for quantitative imaging of $K_{at}$ during biomass combustion in a flat flame [13].

The $K_{at}$ fragments following dissociation of KOH and KCl can, in addition to fluorescence, be detected through absorption techniques. Sorvajärvi et al. developed collinear photofragmentation and atomic absorption spectroscopy (CPFAAS) [14], where a fixed-wavelength diode laser at 766.5 nm was employed to probe the $K_{at}$ fragments, to monitor $K_{at}$, KOH and KCl concentrations during combustion of biomass particles [15]. Based on CPFAAS, which has limited dynamic range, photofragmentation tunable diode laser absorption spectroscopy (PF-TDLAS) was developed by Thorin et al., using a wavelength-tunable diode laser at 769.9 nm to probe the $K_{at}$ fragments, and employed for measurement of K species in biomass combustion [16] and gasification [17]. This technique was also used by Liu et al. in an altered beam configuration to quantify KOH and KCl in a flame point-by-point with a spatial resolution of 1 $mm^3$ [18,19].

Here, we present photofragmentation laser absorption imaging (PF-LAI), which combines photofragmentation of KOH and KCl molecules with LAI of $K_{at}$ for simultaneous, quantitative imaging of $K_{at}$, KOH and KCl. Using a camera frame rate of 0.8 MHz and an imaging domain of 3.8-by-16.4 mm, the $K_{at}$ absorption profiles and the $K_{at}$ fragment decay curves following dissociation of KOH and KCl were measured quasi-simultaneously with an image acquisition rate of 50 Hz before averaging. The technique was demonstrated by quantitative imaging of $K_{at}$, KOH and KCl close to solid biomass fuels, converted in a laboratory methane ($CH_4$)-air flat flame. The fuels investigated in this work were wheat straw and coffee husk, which both are rich in K, but expected to exhibit different release behaviors. Furthermore, the potential of the PF-LAI technique for application in reaction kinetics imaging was demonstrated. The frame rate used in these experiments enabled wide-field imaging of the post-fragmentation temporal evolution of the K fragments, which is related to the local temperature and gas composition.

## 2. Photofragmentation and laser absorption imaging

The principle of the PF-LAI technique is a wide-field extension of PF-TDLAS, which combines tunable diode laser absorption spectroscopy (TDLAS) probing one species, and dissociation of molecular species using photofragmentation (PF), where one of the fragments is the same species probed by TDLAS [16,18]. The intensity of a laser beam propagating in the $z$−direction through an absorbing medium is subject to attenuation, where the relation between the incident intensity $I_0$ and the transmitted intensity $I$ is given by the Beer-Lambert law

$$I(\nu) = I_0(\nu)\exp\left[-\int_0^L k_\nu(\nu)\,\mathrm{d}z\right] + I_{D,0}, \tag{1}$$

where $k_\nu$ ($cm^{-1}$) is the spectral absorption coefficient of the medium, $I_{D,0}$ is the detector background intensity (no laser irradiation), $\nu$ ($cm^{-1}$) is the laser frequency and $L$ (cm) is the absorption path length. The absorption coefficient of a gaseous absorber is given by the product of the analyte mole fraction $x$, gas pressure $P$ (atm), and absorption line strength $S$ ($cm^{-2}$•$atm^{-1}$), or equivalently, the analyte number density $N$ (molecule•$cm^{-3}$) and absorption cross section $\sigma$ (cm•$molecule^{-1}$)

$$k_\nu(\nu) = xPS\psi(\nu) = N\sigma\psi(\nu), \tag{2}$$

where $\psi$ (cm) is the area-normalized line shape function, which is normalized to unity when integrated over all frequencies. By spectral integration, Eq. (2) reduces to

$$k = \int_{-\infty}^{\infty} k_\nu(\nu)\,\mathrm{d}\nu = xPS = N\sigma, \tag{3}$$

which we refer to as the absorption coefficient. The LOS absorbance measured by each camera pixel $i$ is given by

$$A_i = \int_0^{L_i} k\,\mathrm{d}z, \tag{4}$$

and is a projection of the absorption coefficient along the LOS. When the absorption coefficient is non-uniform along the LOS, the spatial information is limited to a LOS average.

The spatial distribution of the absorption coefficient can be resolved using tomographic reconstruction, which generally requires multiple projections along different directions. However, if the absorption coefficient is rotationally symmetric, and the symmetry axis is perpendicular to the laser beam direction, a single projection is sufficient for reconstruction, known as one-dimensional (1D) tomography [12]. The absorption coefficient at radius $j$ is then given by

$$k_j = D_{ij}A_i, \tag{5}$$

where $D_{ij}$ is an inversion matrix. The Abel three-point method inversion matrix was used in this work due to its relative simplicity and computational efficiency [12]. Eq. (5) is mathematically ill-conditioned and is sensitive to measurement noise, especially near the symmetry axis. The noise sensitivity is often reduced through Tikhonov regularization, where $k_j$ is obtained by least-square fitting the system of equations

$$\begin{bmatrix} (D_{ij})^{-1}k_j w_i \\ \beta\partial_{ij}k_j \end{bmatrix} = \begin{bmatrix} A_i \\ 0 \end{bmatrix}, \tag{6}$$

with $k_j$ as open parameter, where $\beta$ is a regularization parameter and $\partial_{ij}$ is a discrete derivative matrix. In this work, a weighting vector $w_i$ has been introduced in Eq. (6) to account for a possible obstruction of the laser beam, by e.g. a sample holder or a biomass sample, to avoid false reconstructions. The weighting vector has a weight of zero for the obstructed pixels and one otherwise. The regularization parameter is chosen to suppress the irregularities in the solution caused by the measurement noise, while keeping the overall structure of the absorption coefficient intact. Inappropriate choice of $\beta$ results in poor noise suppression (under-regularization) or a solution vastly different from the original problem (over-regularization) [20].

Molecules can have dissociative absorption transitions, whose excitation can lead to breaking of the molecular bonds and separation of the molecules into fragments, which can be used to probe properties of the precursor molecules, e.g. using TDLAS. For fragmentation of a target molecule by a fragmentation laser pulse at $t = 0$, and probing of one fragment using TDLAS, the probe laser intensity (PF signal) is given by

$$I_{PF}(t) = I(t)\exp[-\alpha_{PF}(\nu)\cdot f(t)], \tag{7}$$

where $I$ is the pre-fragmentation intensity in Eq. (1) and $\alpha_{PF}$ is the fragment absorbance at $t = 0$. The function $f$ describes the temporal evolution of the fragments due to reactions, which is a function of temperature and gas composition and typically follows an exponential decay on nanosecond (ns) to microsecond (μs) time scales in combustion conditions [21]. When attenuation of the incident pulse energy $E_{in}$ (J) is negligible, the precursor molecule mole fraction $x_M$ can be calculated by [14]

$$x_M = -\ln\left(1 - \alpha_{PF}(\nu)\frac{hcA_f}{\gamma\lambda_f\sigma\psi(\nu)E_{in}}\right)\frac{k_B T}{P\sigma_M\psi_M(\lambda_f)L_f}, \tag{8}$$

where $A_f$ ($m^2$) is the cross-sectional area of the fragmentation beam in the probe volume, $L_f$ (m) is the fragment absorption path length, $\lambda_f$ (m) is the fragmentation laser wavelength, $\gamma$ is the fragmentation efficiency, $\sigma_M$ ($m \bullet molecule^{-1}$) is the absorption cross section of the precursor molecule transition, $\psi_M$ (m) is the line shape function of the molecular transition, $T$ (K) is the gas temperature and $P$ (Pa) is the gas pressure. In Eq. (8), $P$ is given in units of (Pa), and $\sigma$ and $\psi$ are given in units of ($m \bullet molecule^{-1}$) and (m), respectively. The parameters $c$ ($m \bullet s^{-1}$), $h$ ($J \bullet s$) and $k_B$ ($J \bullet K^{-1}$) are the speed of light, Planck's constant and Boltzmann's constant, respectively.

## 3. Materials and methods

### 3.1. Experimental PF-LAI setup

A schematic drawing of the PF-LAI setup (top view and side view) is depicted in Fig. 1. The output beam (diameter 2.2 mm) of a fiber-coupled distributed feedback laser (Nanoplus) at 769.9 nm used to probe $K_{at}$ was expanded to a diameter of 44 mm using a pair of lenses (Thorlabs LB1157-B and LA1353-B). The expanded beam was directed across the outlet of a cylindrical, water-cooled flat flame burner with an inner and an outer section (total diameter 62 mm), parallel to its surface. The inner section of the burner, 38 mm in diameter, was fueled with a premixed $CH_4$-air mixture controlled with mass-flow controllers (MKS GM50A), whereas 5 $L \bullet min^{-1}$ of nitrogen ($N_2$) was supplied to the remaining portion of the burner to form an inert shroud. The flow rates of $CH_4$ and air were 0.319 and 4.681 $L \bullet min^{-1}$, respectively, corresponding to a fuel–air equivalence ratio (ϕ) of 0.65, which produced a stable flat flame with a temperature of around 1600 K, measured using wavelength modulation absorption spectroscopy of water vapor [22]. The burner was mounted on two linear translation stages for horizontal and vertical adjustment of the imaging domain. A platinum (Pt) plate with a diameter of 6 mm, suspended 5 mm above the burner surface using 0.25 mm thick Pt wires, was used as a sample holder. The flame parameters are summarized in Table 1.

After passing through the flame, the laser beam was focused by a third lens, and the laser beam intensity was recorded with a high-speed

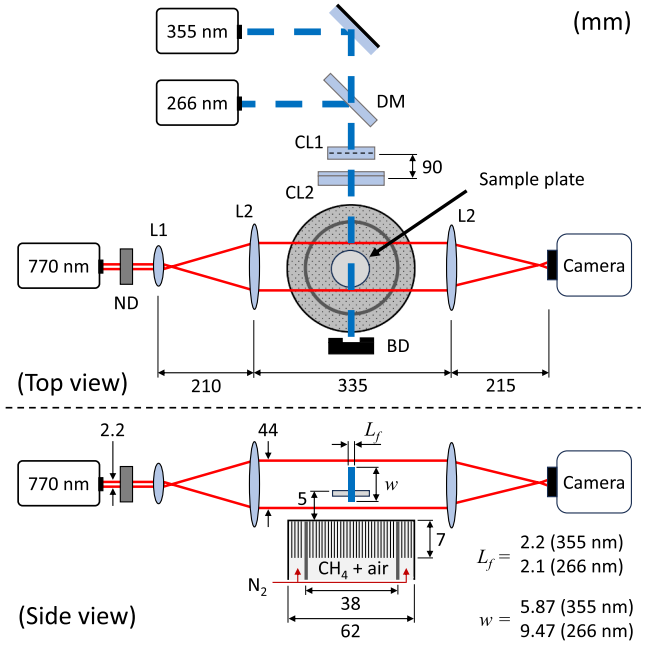


**Fig. 1.** Schematic drawings (top view and side view) of the PF-LAI system, including the flat flame burner and showing the location of the sample plate made of platinum. ND – Neutral density filter, L – lens, CL – cylindrical lens, DM – dichroic mirror.

**Table 1**
Flame parameters.

| $CH_4$ ($L \bullet min^{-1}$) | Air ($L \bullet min^{-1}$) | ϕ | Temperature (K) | $N_2$ ($L \bullet min^{-1}$) |
|---|---|---|---|---|
| 0.319 | 4.681 | 0.65 | 1600 | 5 |

camera (Photron NOVA S16). The output beams of two pulsed third- and fourth harmonic Nd:YAG lasers at 355 and 266 nm (CryLas FTSS 355-300 and FQSS 266-200), with beam diameters of 2.2 and 2.1 mm, respectively, served to fragment the KOH and KCl molecules. The beams of these fragmentation lasers were combined into a common beam path using a dichroic mirror (Semrock FF310-Di01-25x36) and expanded to sheets using a pair of cylindrical lenses (Thorlabs LK4372-UV and LJ4395-UV). The energy distributions of the 355 nm and 266 nm laser sheets followed Gaussian profiles with $1/e^2$ (radial) widths of 5.87 and 9.47 mm, with pulse energies of 112.3 and 19.1 μJ, respectively. These sheets were incident parallel to the burner surface at a right angle to the probe laser beam, with beam centers overlapping above the burner outlet and sample plate, on the symmetry axis. The accuracy of the PF-TDLAS technique in the LOS configuration was assessed in previous works to be within 10 % for all three species [16,23,24].

### 3.2. Imaging process

For K species imaging, the probe laser frequency was scanned by applying a 100 Hz sawtooth modulation of the laser current with a peak-to-peak amplitude corresponding to a frequency tuning range of 4.68 $cm^{-1}$, covering the full $K_{at}$ absorption profile. The scan briefly extended below lasing threshold to measure the background intensity, which was subtracted from the intensity spectra. The camera acquisition was synchronized with the probe and fragmentation lasers and one acquisition comprised two probe laser scans. First, a partial scan containing the PF signals due to the two fragmentation laser pulses with temporal separation of 92 μs, followed by a full scan of the $K_{at}$ absorption profile without PF signals. A typical camera acquisition of a single pixel recorded during conversion of a KCl salt sample is presented in Fig. 2(a).

The camera frame rate was set to 825 kHz, which resulted in an average spectral resolution of $6.60 \bullet 10^{-4}$ $cm^{-1}$ for the $K_{at}$ absorption profile and a temporal resolution of 1.2 μs for the PF signals. The imaging region was set to 32-by-128 pixels, the maximum for the selected frame rate. The spatial resolution was determined to 122 μm in the vertical direction and 129 μm in the horizontal direction using a wire mesh with 1.0 mm spacing and 0.5 mm wire thickness, as described in our previous work [13], resulting in an imaging domain of 3.8-by-16.4 mm. The exposure time was set to 0.2 μs, which, in combination with a neutral density filter at the probe laser output, maximized the intensity without saturating the camera pixels. The probe laser and camera parameters are summarized in Table 2.

A temporal average of 25 consecutive acquisitions (0.5 s) was collected, followed by spatial averaging of each pixel with a 3-by-3 px average on every frame. Voigt profiles were fitted to the recorded $K_{at}$ absorption spectra from every pixel and the radially resolved $K_{at}$ concentrations were obtained by least-square fitting of Eq. (6). By comparison to the unregularized result, a regularization parameter of $\beta = 0.2$ was found to yield a sufficient regularization without significantly altering the overall structure. The KOH and KCl concentrations were calculated from the PF signal absorbances using Eq. (8) and absorption cross section data presented by Weng et al. [25], and the fragment decay curves were fitted by a single exponential function as seen in Fig. 2(b). The fragment absorption path length was equal to the fragmentation laser beam diameters before expansion (2.1 and 2.2 mm), as implied by the laser beam orientations in Fig. 1. Hence, tomographic reconstructions were not necessary to obtain the radial KOH and KCl concentrations.

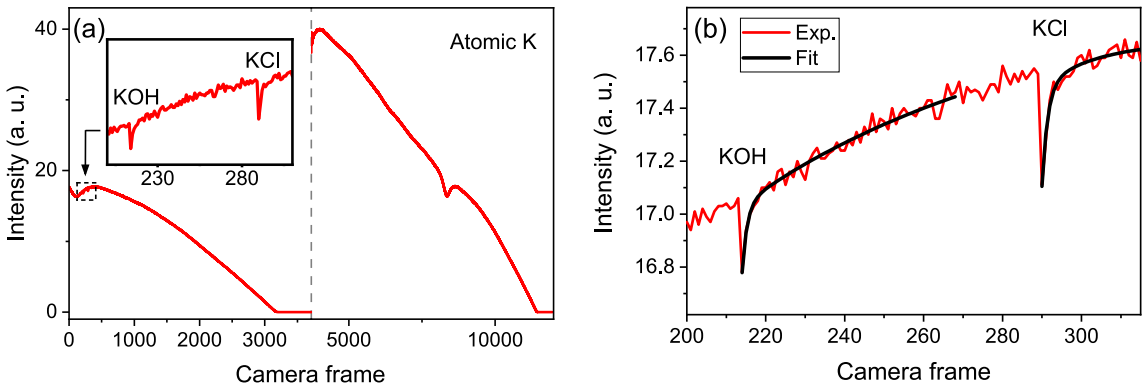


**Fig. 2.** (a) Typical absorption signal recorded by a single pixel during one acquisition. The inset shows the PF signals due to fragmentation of KOH and KCl. (b) Typical PF signals (red) with curve fits (black).

**Table 2**
Probe laser and camera parameters.

| Parameter | Value |
|---|---|
| Laser scan rate | 100 Hz |
| Center wavelength | 769.9 nm |
| Frame rate | 825 kHz |
| Exposure time | 0.2 μs |
| Active pixels | 32 × 128 px |
| Spatial resolution (vertical) | 122 μm |
| Spatial resolution (horizontal) | 129 μm |
| Temporal resolution (PF) | 1.2 μs |
| Spectral resolution | $6.60 \bullet 10^{-4}$ $cm^{-1}$ |
| Acquisition rate (final image) | 50 Hz |

### 3.3. Fuels

Samples of KCl salt were investigated as a reference case to validate the technique. Furthermore, two different biomass fuels were studied in this work: coffee husk (CH) and wheat straw (WS). The WS samples, originally in the form of pellets with a diameter of 6.5 mm, were cut to particles with a length of 5.5 mm and ground to the shape of a dome. Since CH pellets swell during combustion, which causes the sample to fall off the sample plate, CH flakes of similar size as the WS particles were used. The elemental compositions of the two fuels are presented in Table 3. While both contain a high amount of K, the key difference is the content of chlorine (Cl), which is known to promote K release and will probably bind to atomic K [26]. In the absence of available Cl, K is most likely to form KOH. Therefore, higher levels of gaseous KCl release are to be expected from the WS than from CH sample.

**Table 3**
Elemental compositions of coffee husk and wheat straw.

| | Coffee Husk | Wheat Straw |
|---|---|---|
| LHV[a] (MJ/kg dry) | 17.8 | 16.6 |
| Moisture[b] (wt.-% rec.) | 10 | 10 |
| Ash (wt.-% dry) | 5.3 | 9.05 |
| **Ultimate analysis (wt.-% dry)** | | |
| C | 47.9 | 44.28 |
| H | 6.0 | 5.62 |
| N | 1.2 | 0.88 |
| O | 39.5 | 40.00 |
| S | 0.1 | 0.139 |
| **Main ash-forming elements (mg/kg dry)** | | |
| Cl | 535 | 3510 |
| Al | 298 | 701 |
| P | 1000 | 882 |
| Fe | 312 | 546 |
| Ca | 4080 | 5110 |
| K | 20,200 | 14,600 |
| Mg | 1090 | 1130 |
| Na | 56 | 214 |
| Si | 657 | 22,100 |

[a] Lower heating value, dry substance.
[b] Wt.-% of fuel as received.

## 4. Results

### 4.1. KCl salt sample

First, a solid KCl salt sample was investigated as a reference case. Fig. 3 shows typical (a) $K_{at}$, (b) KOH and (c) KCl concentration images during conversion of the KCl sample in the $CH_4$-air flame, with the sample plate depicted in grey. Tomographic reconstruction was applied to obtain the radial $K_{at}$ concentrations. Since this case is a relatively stationary process [16], image sections were collected at three different heights in the flame during conversion of one sample and combined to a single image. Between each image section, the imaging region was shifted vertically by 3 mm, where the seams of the composite image are indicated by the dashed lines in Fig. 3. The vertical axes represent the height above the plate (HAP) and the horizontal axes show the radial distance from the plate center. Due to the imposed symmetry of the 1D tomography method for reconstruction of the radial $K_{at}$ concentration in Fig. 3(a), only half of the LOS absorption image is needed. The dash-dotted line represents the axis of symmetry that separates the two reconstructions using the respective half of the image. The lower bounds of the color scales represent typical noise levels.

The $K_{at}$ and KCl concentrations peak close to the sample plate and decline as a function of HAP, with the former declining more rapidly. KOH first appears above a HAP of 3 mm, most probably due to decomposition of KCl. Furthermore, KOH shows a discontinuous step-increase around HAP 3 mm (see also Fig. 4b), by coincidence exactly at the seam between the two lower image sections. Given the fact that the KOH concentration was close or below the detection limit in the lowest image section, and since the detection limits for KOH and KCl increase towards the edges of each section in the vertical direction due to the energy distributions of the fragmentation beams, this steep incline of KOH could not be detected in Fig. 3(b). $K_{at}$ accumulates at the plate edges and extends below the plate, outside of the imaging domain, as an effect of flow recirculation due to obstruction by the sample plate [16]. The $K_{at}$ distributions close to the plate differ between the two reconstructions, a result of a lack of symmetry in the absorbance profile that is likely due to a non-uniformly distributed sample on the plate, making 1D tomography insufficient in resolving the spatial variations. Nonetheless, the distribution depicted in the left reconstruction in Fig. 3 (a) is in good agreement with results from our previous work where cylindrical symmetry was fulfilled [13]. At heights from around 3 mm, a

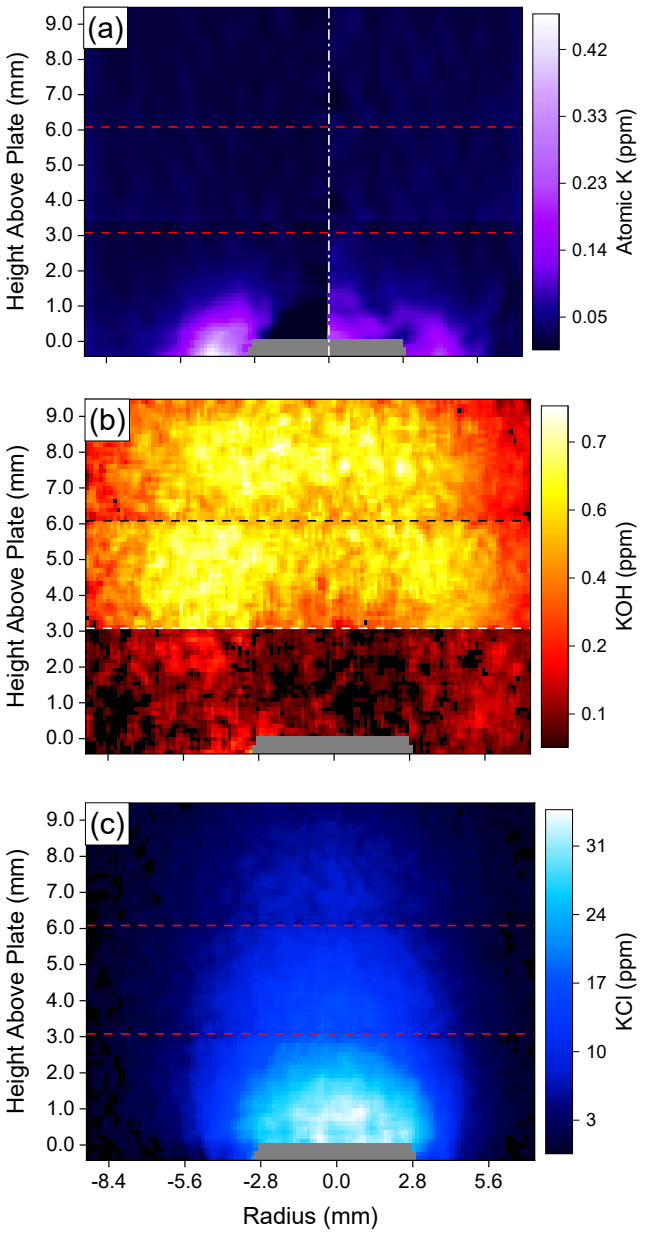


**Fig. 3.** Concentration images of gaseous K species distributions during conversion of a KCl salt sample in the $CH_4$/air flat flame. (a) Atomic potassium, $K_{at}$, (b) potassium hydroxide, KOH, and (c) potassium chloride, KCl. Tomographic reconstruction was used only for atomic K. The grey area at the bottom center depicts the sample plate.

symmetric absorbance profile was observed.

A comparison between the LOS-averaged K species concentrations measured in the present work (lines) and previous point-measurements (markers) [16] is shown in Fig. 4, where the dashed lines represent the average noise levels in the KOH and KCl measurements. A good qualitative agreement in the concentration curves is observed, with emphasis on $K_{at}$ and KCl. The difference in absolute K species concentrations (note the different vertical axes) is the result of different flame conditions (higher $\phi$ and flow rates), which, in the present work, were chosen to obtain $K_{at}$ concentrations that maximize the PF signal contrast. The vertical shifts in the KOH (~2 mm) and KCl (<1 mm) concentration curves could be related to either a change in temperature gradient due to the different flame conditions, or a difference in decomposition rates of KCl to KOH. Another reason for the KCl shift could also be the limited spatial resolution in the previous work (markers) due to the finite beam

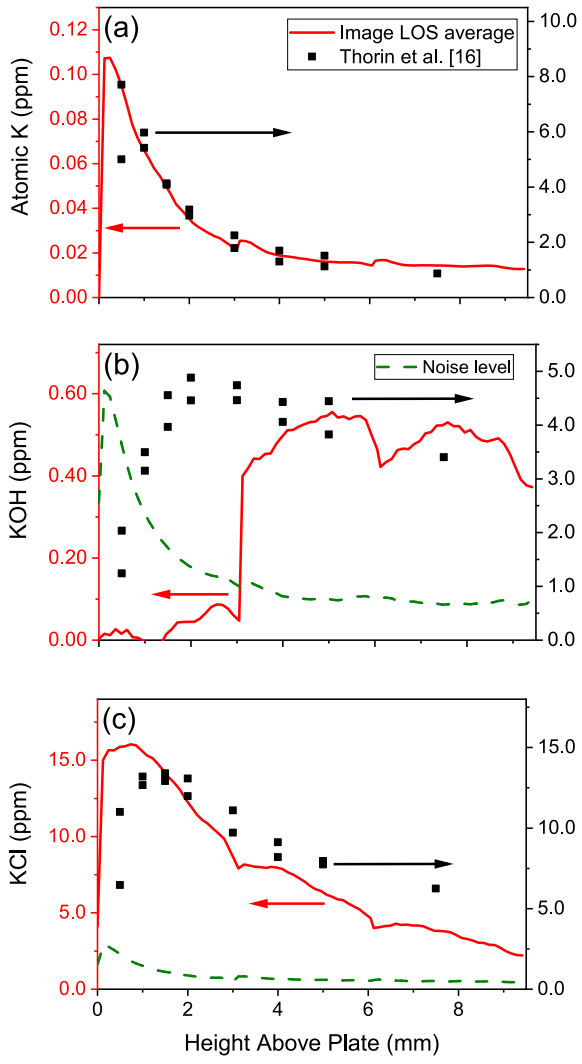


**Fig. 4.** Line-of-sight averaged K species concentrations measured in the present study (lines) and in previous work (markers) [16]. (a) Atomic potassium, $K_{at}$, (b) potassium hydroxide, KOH, and (c) potassium chloride, KCl. The green, dashed lines represent average noise levels.

size [13,16].

### 4.2. Biomass samples

Images of typical K species concentrations from a CH sample (depicted in green), during the devolatilization (left column) and char burning (right column) stages of the same sample are presented in Fig. 5. As for the KCl salt sample, the tomographic reconstruction method was applied only for $K_{at}$, while it was not necessary to obtain the radial KOH and KCl concentrations owing to the experimental configuration with the thin UV laser sheets perpendicular to the probe laser beam. Here, the vertical axes represent the height above the sample before conversion and the horizontal axes are the radial distances, centered to the $K_{at}$ absorption profile. By comparing the left and right columns, a change in the shape of the sample during the conversion process is evident.

As seen in Fig. 5, the K species are present in a plume close to the sample. While the $K_{at}$ and KOH concentrations were higher in the devolatilization stage than during char burning, the opposite was observed for KCl, Fig. 5(c), which could not be detected above the noise level during devolatilization. Most of the Cl release is expected to occur during devolatilization [27], and the same holds for the majority of inorganic K, which may be the main constituent of the K in the fuel [28].

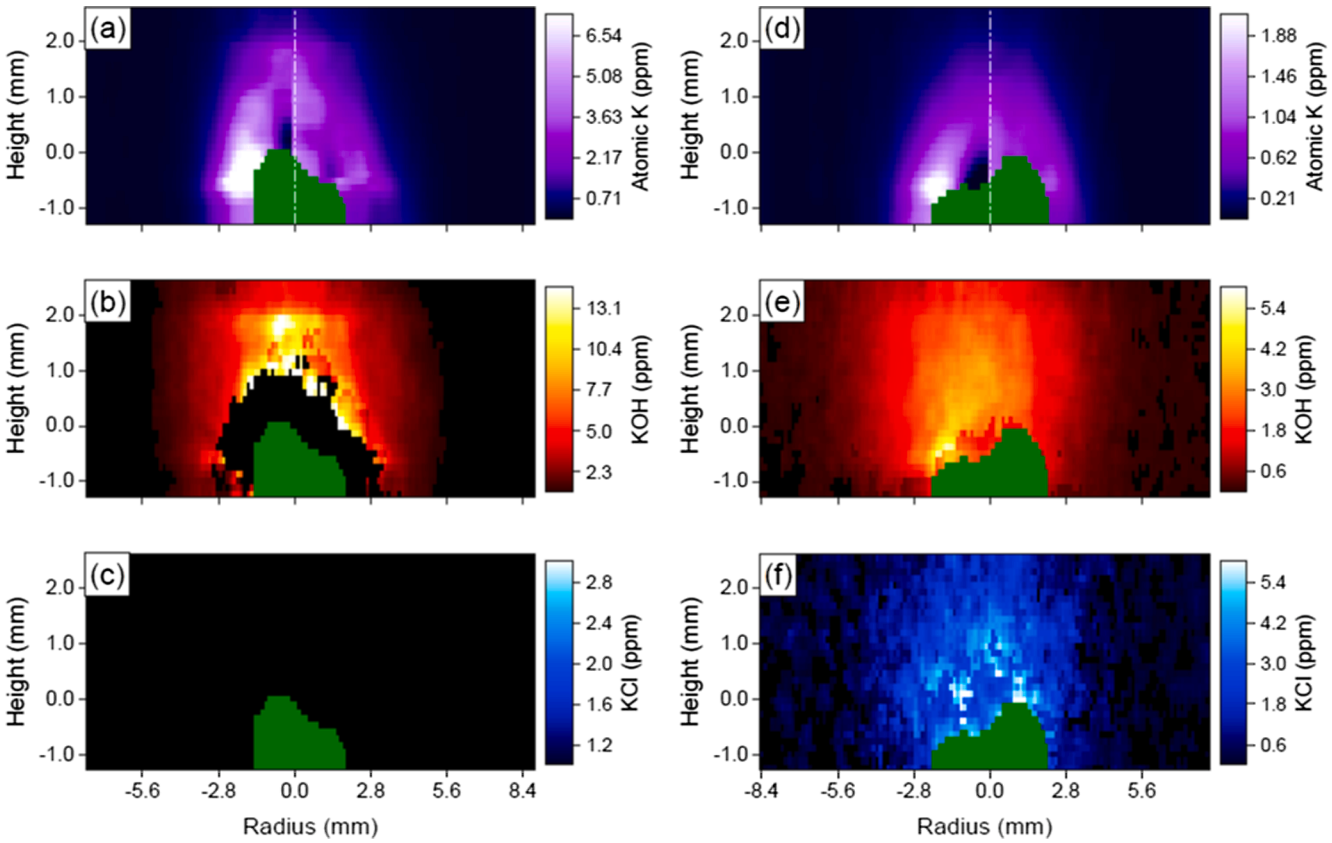


**Fig. 5.** Typical K species concentration images during the devolatilization (left column) and char burning (right column) stages for a coffee husk sample. (a, d) Atomic potassium, $K_{at}$, (b, e) potassium hydroxide, KOH, and (c, f) potassium chloride, KCl. Tomographic reconstruction was used only for atomic K. The green area represents the biomass particle.

However, it is likely that the temperature of the biomass particle during devolatilization was still too low (<923 K) for direct KCl evaporation, and the Cl was instead released in other forms, such as HCl or $CH_3Cl$ [8]. The noise levels of KOH and KCl reduce from the devolatilization to the char burning stage solely due to the decrease in $K_{at}$ concentration, which results in a higher light transmission due to the lower absorption. The reduction in light transmission due to soot was negligible in these experiments. The black region close to the sample in Fig. 5(b) contained KOH signals below the noise level (~2 ppm), which indicates an initial release entirely in the form of $K_{at}$, probably through decomposition of char-K [7]. It should be emphasized that the absence of KOH and KCl close to the sample is in good agreement with the work by Liu et al., where no KOH or KCl could be detected during devolatilization of wood [19]. In the char burning stage, the particle temperature is higher, enabling K evaporation directly as KCl and KOH, the latter mainly from the decomposition of $K_2CO_3$ generated from char-K oxidation [18].

Fig. 6 depicts typical K species concentration images during devolatilization and char burning of a single WS sample (depicted in green). As in the case of the CH sample, the vertical axis shows the height above the sample before conversion and the horizontal axis is centered to the $K_{at}$ absorption profile.

For the WS sample, neither KOH nor KCl could be detected above the noise levels during the devolatilization stage, and the $K_{at}$ concentration profile shows a clear difference to the CH sample. Here, $K_{at}$ is distributed in a cylindrical shell around the particle, with the highest concentrations at a radius of about 6 mm. This cylindrical shell distribution during devolatilization of WS was also observed in a previous experiment, and is believed to coincide with the reaction zone of the sooty flame emerging during the devolatilization stage [13]. Similarly as for CH, the K is likely released through decomposition of char-K during devolatilization. It should be noted that the difference in sample types between CH and WS (flakes and ground pellet, respectively) cannot be excluded as the reason for the difference in their $K_{at}$ distributions. In the char burning stage, a similar $K_{at}$ distribution as for the CH sample was observed, seemingly extending wider in the radial direction. Still, basically no KOH above noise level could be detected. On the other hand, a high amount of KCl was measured during this stage, approximately a factor of four higher than for the CH sample. These concentration levels are in good agreement with the levels reported by Liu et al. [18] and can be attributed to the high Cl content in WS. The decrease in KCl concentration with height above the sample may indicate the onset of KOH formation, see Fig. 6(e).

### 4.3. PF signal decay rates

Fig. 7 presents the fitted PF signal decay time constants for the cases with highest contrast and most prominent spatial variations: (a) KCl salt sample, (b) CH char burning and (c) WS char burning. For the CH case, the decay time constant of the PF signal following fragmentation by the 355 nm laser is presented, while the other two cases correspond to fragmentation by the 266 nm laser. The uncertainty in the decay time constant presented in Fig. 7(a) was estimated using a 95 % confidence interval obtained from the fitting routine. The resulting relative uncertainty along the vertical center line (radius = 0) ranged from 15 % in the high signal region, to 45 % in the low signal region.

Common to all three cases in Fig. 7 is a lower decay time constant, i.

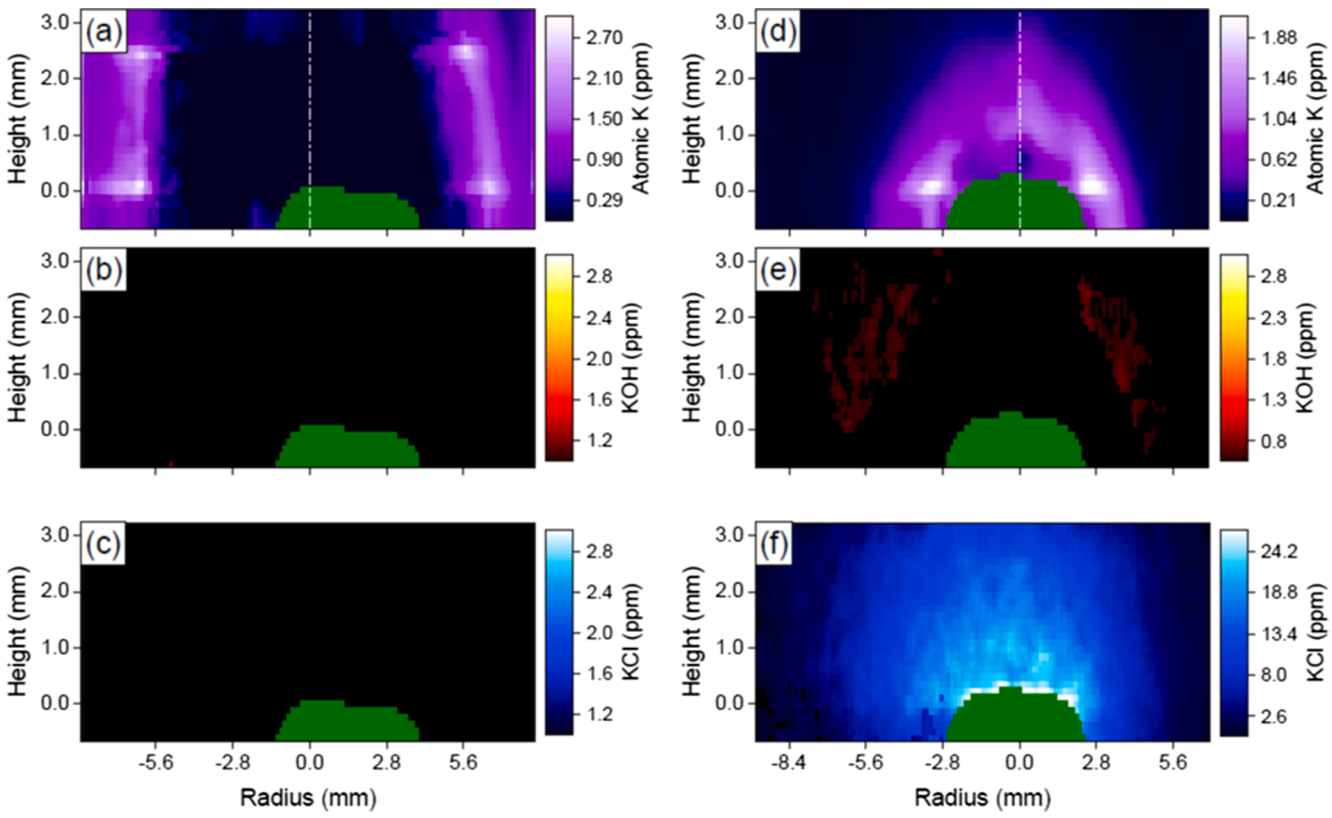


**Fig. 6.** Typical K species concentration images during the devolatilization (left column) and char burning (right column) stages for a wheat straw sample. (a, d) Atomic potassium, Kat, (b, e) potassium hydroxide, KOH, and (c, f) potassium chloride, KCl. Tomographic reconstruction was used only for atomic K. The green area represents the biomass particle.

e. a faster decay, close to the sample and an increasing time constant with increasing distance from the sample. The similarities in time constants indicate that there are no drastic differences in K gas-phase chemistry between the samples. The recombination of the K fragments is a complex process involving several reactions [29] and the decay time constant depends on both temperature and gas composition, such as oxygen ($O_2$). Previous work by Viljanen et al., indicated that the decay time constant is more sensitive to temperature than to $O_2$ concentration [21]. However, the work by Viljanen et al. was conducted in different conditions, notably at lower temperatures, which may result in different K fragment chemistry compared to that of the present work. In the thesis of Thorin, it was shown that the main reaction involving $O_2$ plays a lesser role in the conditions produced by the $CH_4$-air flame, and in fuel-rich conditions, the PF signal decay was affected by reactions with $CO_2$, carbon monoxide (CO) and hydrogen chloride (HCl) [30]. In the present work, there is a lack of information on the gas composition and local gas temperature to obtain further chemical information from the decay time constants using reaction kinetics. Nonetheless, assuming similar decay rate dependencies as previous works [14,21], the images of time constants are consistent with the expected temperature distributions in these experiments [13] and could serve as a qualitative estimate of the temperature gradients.

## 5. Conclusions

Photofragmentation laser absorption imaging has been introduced for simultaneous, quantitative wide-field imaging of gaseous $K_{at}$, KOH and KCl with high spatial and temporal resolution. The technique was demonstrated by investigating the conversion of KCl salt and biomass samples in a laboratory flat flame. The K species concentrations measured during conversion of KCl salt showed good qualitative agreement with our previous works, with KCl as the dominating species. The spatial distributions of gaseous K species around coffee husk particles during combustion were measured for the first time and compared to those obtained for wheat straw samples. During the devolatilization stage, K was mostly released as $K_{at}$, but the spatial distributions were different for the two fuels. For coffee husk, $K_{at}$ was localized close to the particle, while for wheat straw, $K_{at}$ was distributed in a cylindrical shell around the sample. During char conversion, K release was mainly in the form of KOH and KCl for coffee husk, while only KCl was detected for the wheat straw sample, albeit at significantly higher levels than for coffee husk, due to the much higher Cl content in wheat straw. The K fragment decay following fragmentation of KOH and KCl was imaged with a temporal resolution of 1.2 μs and used to spatially map the decay rates. Although only used qualitatively here, this shows the potential for wide-field imaging of K reaction kinetics employing PF-LAI. For more detailed studies and utilization of reaction kinetics, e.g., to obtain chemical information, the dependencies of the decay rates for the prevailing conditions must be determined.

## CRediT authorship contribution statement

**Emil Thorin:** Writing – review & editing, Writing – original draft, Visualization, Validation, Software, Methodology, Investigation, Formal analysis, Data curation, Conceptualization. **Florian M. Schmidt:** Writing – review & editing, Visualization, Methodology, Formal

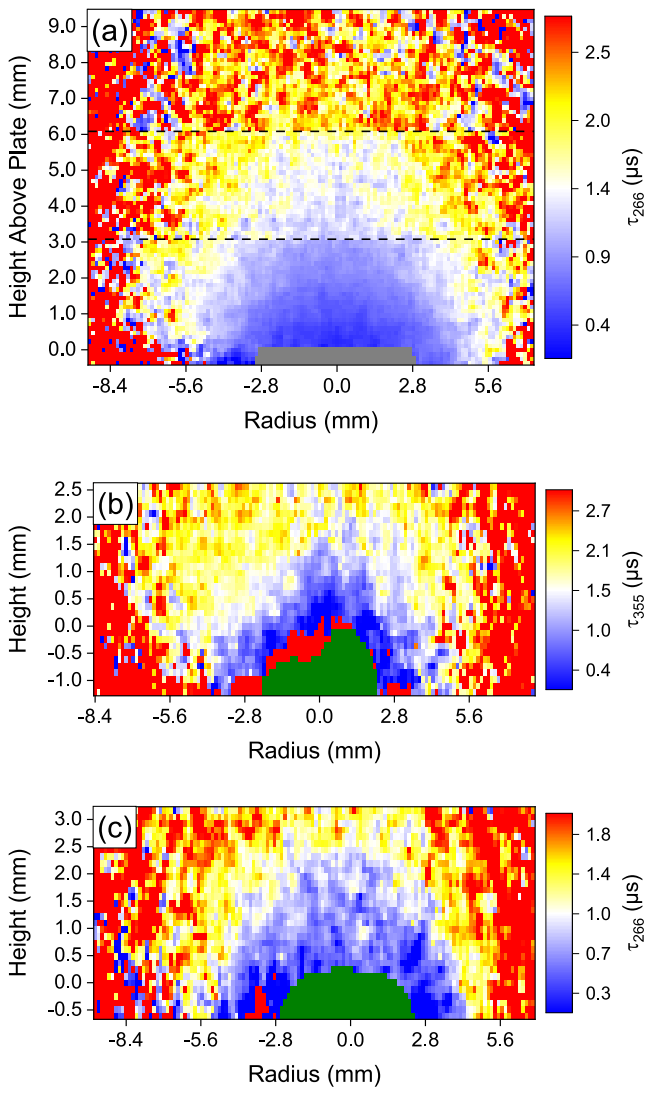


**Fig. 7.** Fitted K fragment decay time constants. (a) KCl salt sample, (b) coffee husk sample during char burning, and (c) wheat straw sample during char burning. The grey area in (a) depicts the sample plate and the green area in (b) and (c) represents the biomass particle.

analysis, Conceptualization.

## Declaration of competing interest

The authors declare that they have no known competing financial interests or personal relationships that could have appeared to influence the work reported in this paper.

## Acknowledgments

The authors acknowledge financial support from the Swedish Energy Agency through both the Swedish Gasification Centre (SFC) and project no. 36160-1, the Kempe Foundations (JCK-1316 and JCK-2025), as well as the Swedish strategic research program Bio4Energy.

## Data availability

Data will be made available on request.

## References

[1] Kemper J. Biomass and carbon dioxide capture and storage: A review. Int J Greenh Gas Con 2015;40:401–30.
[2] Azar C, Johansson DJA, Mattsson N. Meeting global temperature targets—the role of bioenergy with carbon capture and storage. Environ Res Lett 2013;8(3):034004.
[3] Niu Y, Tan H, Se H. Ash-related issues during biomass combustion: Alkali-induced slagging, silicate melt-induced slagging (ash fusion), agglomeration, corrosion, ash utilization, and related countermeasures. Prog Energ Combust 2016;52:1–61.
[4] Abioye KJ, Harun NY, Sufian S, Yusuf M, Jagaba AH, Ekeoma BC, et al. A review of biomass ash related problems: Mechanism, solution, and outlook. J Energy Inst 2024;112:101490.
[5] Wang Z, Liu S, Weng W, He Y, Aldén M, Li Z. Alkali metal release in thermochemical conversion of biomass and coal: Optical measurements and modeling. Prog Energy Combust Sci 2024;100:101131.
[6] van Eyk PJ, Ashman PJ, Alwahabi ZT, Nathan GJ. Quantitative measurement of atomic sodium in the plume of a single burning coal particle. Combust Flame 2008; 155(3):529–37.
[7] Liu Y, Wang Z, Xia J, Vervisch L, Wan K, He Y, et al. Measurement and kinetics of elemental and atomic potassium release from a burning biomass pellet. Proc Combust Inst 2019;37(3):2681–8.
[8] Weng W, Aldén M, Li Z. Insight into KOH and KCl release behavior of burning wood and straw pellets using quantitative in situ optical measurements. Proc Combust Inst 2022.
[9] Daily JW. Laser induced fluorescence spectroscopy in flames. Prog Energy Combust Sci 1997;23(2):133–99.
[10] Hanson RK, Seitzman JM, Paul PH. Planar laser-fluorescence imaging of combustion gases. Appl Phys B 1990;50(6):441–54.
[11] Wei C, Pineda DI, Goldenstein CS, Spearrin RM. Tomographic laser absorption imaging of combustion species and temperature in the mid-wave infrared. Opt Express 2018;26(16):20944–51.
[12] Cai W, Kaminski CF. Tomographic absorption spectroscopy for the study of gas dynamics and reactive flows. Prog Energy Combust Sci 2017;59:1–31.
[13] Thorin E, Paiva EM, Schmidt FM. Quantitative tomographic laser absorption imaging of atomic potassium during combustion of potassium chloride salt and biomass. Anal Chem 2023;95(2):1140–8.
[14] Sorvajärvi T, Toivonen J. Principles and calibration of collinear photofragmentation and atomic absorption spectroscopy. Appl Phys B 2013;115 (4):533–9.
[15] Sorvajarvi T, DeMartini N, Rossi J, Toivonen J. In situ measurement technique for simultaneous detection of K, KCl, and KOH vapors released during combustion of solid biomass fuel in a single particle reactor. Appl Spectrosc 2014;68(2):179–84.
[16] Thorin E, Zhang K, Valiev D, Schmidt FM. Simultaneous detection of K, KOH, and KCl in flames and released from biomass using photofragmentation TDLAS. Opt Express 2021;29(26):42945–61.
[17] Thorin E, Sepman A, Ögren Y, Ma C, Carlborg M, Wennebro J, et al. Quantitative real-time in situ measurement of gaseous K, KOH and KCl in a 140 kW entrained-flow biomass gasifier. Proc Combust Inst 2023;39(1):1337–45.
[18] Liu S, Weng W, Wang Z, He Y, Aldén M, Li Z. A TDLAS-based photofragmentation method for spatially resolved measurement of KOH and KCl as well as its application in biomass combustion processes. Fuel 2024;357:130077.
[19] Liu S, Weng W, He Y, Aldén M, Wang Z, Li Z. Experimental exploration of potassium compounds in the vicinity of a burning biomass pellet: From near-surface to downstream. Proc Combust Inst 2024;40(1):105583.
[20] Daun KJ, Thomson KA, Liu F, Smallwood GJ. Deconvolution of axisymmetric flame properties using Tikhonov regularization. Appl Opt 2006;45(19):4638–46.
[21] Viljanen J, Sorvajärvi T, Toivonen J. In situ laser measurement of oxygen concentration and flue gas temperature utilizing chemical reaction kinetics. Opt Lett 2017;42(23):4925–8.
[22] Qu Z, Ghorbani R, Valiev D, Schmidt FM. Calibration-free scanned wavelength modulation spectroscopy–application to $H_2O$ and temperature sensing in flames. Opt Express 2015;23(12):16492–9.
[23] Qu Z, Steinvall E, Ghorbani R, Schmidt FM. Tunable diode laser atomic absorption spectroscopy for detection of potassium under optically thick conditions. Anal Chem 2016.
[24] Thorin E, Schmidt FM. TDLAS-based photofragmentation spectroscopy for detection of K and KOH in flames under optically thick conditions. Opt Lett 2020; 45(18):5230–3.
[25] Weng W, Brackmann C, Leffler T, Aldén M, Li Z. Ultraviolet absorption cross sections of KOH and KCl for nonintrusive species-specific quantitative detection in hot flue gases. Anal Chem 2019;91(7):4719–26.
[26] Baxter LL, Miles TR, Miles TR, Jenkins BM, Milne T, Dayton D, et al. The behavior of inorganic material in biomass-fired power boilers: field and laboratory experiences. Fuel Process Technol 1998;54(1):47–78.
[27] Fagerström J, Steinvall E, Boström D, Boman C. Alkali transformation during single pellet combustion of soft wood and wheat straw. Fuel Process Technol 2016;143: 204–12.
[28] Liu Y, Wan K, He Y, Wang Z, Xia J, Cen K. Experimental study of potassium release during biomass-pellet combustion and its interaction with inhibitive additives. Fuel 2020;260:116346.
[29] Glarborg P, Marshall P. Mechanism and modeling of the formation of gaseous alkali sulfates. Combust Flame 2005;141(1):22–39.
[30] Thorin E. Quantitative laser diagnostics of gas-phase potassium species in biomass combustion and gasification. Umeå University; 2023.